Improvement of electrical properties of ITO thin films by melt-free ultra-short laser crystallization

N Farid*[1], A Sharif[1], R K Vijayaraghavan[2], M Wang[3], H Chan[4], A Brunton[4], P McNally[2], K Choy[3], and G M O'Connor[1]

[1]National Centre for Laser Applications (NCLA), School of Physics, National University of Ireland Galway, Ireland

[2]Advanced Processing Technology Research Centre (APT), Nanomaterials Processing Laboratory, School of Electronic Engineering, Dublin City University, Ireland

[3]Institute for Materials Discovery, University College London, UK

[4]M-Solv Ltd. Kidlington, Oxford, UK

E-mail: nazar.farid@nuigalway.ie

Abstract. We describe a novel solid state crystallisation method for optimising a thin film transparent conductive oxide when deposited on flexible polymer substrates. The method is based on ultra-short non-thermal laser sintering of ITO thin films. In this study, we used commercial ITO thin films deposited on a flexible PET substrate with a relatively low melting temperature compared with ITO on glass. We demonstrate the use of laser scanning with high pulse overlapping at a fluences seven times less than the threshold required for melting/damage of ITO. The results confirm that the sheet resistance of the ITO thin films can be reduced by up to 25 % after laser scanning. There is no reduction in optical transparency observed in laser treated samples. Surface morphology and XRD analyses confirm the improvement in crystallite sizes by laser sintering, resulting in a greater than 37% increase in grain size due to enhanced crystallization. Comparison of experimental and simulation based on a delayed two temperature model confirms that ITO thin film crystallization occurred at about one-third of the melting temperature of ITO.

1. Introduction

Indium tin oxide (ITO) is an n-type degenerate semiconductor with a wide band gap. Its high electrical conductivity ($<10^{-5}$ Ω cm), good optical transparency in the visible (<85%) and near infrared regions, and good adhesion to many types of substrates make it crucial in a wide variety of applications [1]. It has been widely used as a transparent conducting layer in modern optoelectronic technology such as organic light emitting devices (OLEDs) [2], transparent touch flat panel displays (FPDs) [3], touch sensors[4] and solar cells [5]. This conducting transparent oxide mainly serves as an electrode and often as an antistatic electromagnetic interference shield or an electric heater in flat panel displays (FPDs) [6]. It has been used as an Ohmic contact material because it has high surface current [7]. The electrical properties of ITO depend on its atomic arrangement, composition, surface structure and on the amorphous and crystalline nature of ITO film. ITO exhibits favourable properties such as low resistivity and high optical transparency in the crystalline state but not in the amorphous phase.

ITO thin films can be deposited by chemical vapour deposition [8], evaporation [9], spray pyrolysis [10], and commercially used magnetron sputtering [11] techniques. All these techniques require a deposition temperature of at least 300-500 °C; higher temperatures (400–700 °C) are required for further annealing to reduce the resistivity and to achieve improved transparency. The requirement for high

[1] To whom any correspondence should be addressed.

temperature limits the use of heat sensitive polymers as substrate materials [12]. In most of the applications, the ITO materials are first sputtered/coated in the amorphous phase on the substrate and then thermally annealed to at least 300 °C to change to the crystalline state [13].

Lasers have become an emerging and alternative tool for material processing and industrial manufacturing; high power short and ultra-short pulse lasers with MHz repetition rates are set to transform micro- and nano-scale fabrication. Laser technology has replaced conventional and rapid high temperature thermal annealing as in the case of Si crystallization [14]. Excimer [15] and nanosecond lasers [15] have also been investigated in ITO crystallization; the crystallized phase results from melting, the thermal budget for which is not suitable for application on heat sensitive flexible substrates. On the other hand, ultrashort lasers are promising in material processing because of their extremely short pulse durations which offer a smaller heat affected zone (HAZ) and thermal damage to the substrate compared to nanosecond laser pulses. Recently ultra-short lasers have also been used for selective ablation [16], patterning [17, 18] and direct laser crystallization [19]. A two-step method was also used for crystalline indium tin oxide (c-ITO) patterns on amorphous ITO (a-ITO) thin films by femtosecond laser irradiation followed by chemical etching [20].

In most of the applications, ITO thin film is deposited on a suitable substrate (i.e. glass or polyethylene terephthalate (PET)) and then crystallized and patterned to form complex and multifunctional electronic circuits. PET being transparent, flexible, lightweight, and cost-effective is one of the candidates in flexible display technology [21]. However, the lower melting temperature of PET does not allow for the high-temperature thermal treatments required for ITO crystallization. Therefore, crystallization of ITO on PET must be carried out at temperatures below 200 °C which is insufficient to optimise ITO layers with good electrical conductivity and transparency [22]. Thus, a low temperature process is needed. In this work, we have developed a low temperature ultra-short laser annealing process to improve the electrical properties of ITO films on heat sensitive substrates.

2. Experimental details

As received commercial ITO thin films (Visiontek) deposited on 0.5 mm thick PET substrates were used as a target material. Two different ITO thicknesses of 50 nm and 100 nm deposited on PET were investigated to enhance the conductivity by ultra-short laser treatment. A femtosecond laser of pulse duration 500 fs at a wavelength of 1030 nm which can operate from single pulse to 300 kHz was used for ITO crystallization. The sample position was controlled using a high precision 3D computer-controlled stage (Aerotech). The sample was scanned using industrial grade Galvo scanning system (Scanlabs). The scanning system controls the pulse to pulse overlap on the sample by adjusting the speed of steering mirrors of galvanometer-based beam scanning system. Optical and scanning electron microscopy (SEM), and atomic force microscopy (AFM) were utilized for analysing the surface morphology of the laser scanned area and single pulse crater depth profiles. The Van der Pauw method was used to measure the sheet resistance and electrical conductivity of ITO before and after the laser scanning. The crystallinity of the ITO films was quantified using Cu-Kα X-ray diffraction (XRD); λ = 1.54 Å. Optical transmission was measured using UV-Vis spectrometry. The laser spot diameter at the focused position and the damage threshold were calculated experimentally using the Liu method [23];

$$D^2 = 2\omega_0^2 ln\left(\frac{\varphi_0}{\varphi_{th}}\right), \quad (1)$$

where, $\varphi_0 = 2E_p/\pi\omega_0^2$ and φ_{th} are the applied and threshold fluence, ω_o is beam waist radius of the Gaussian shaped beam at the focus, E_p is absorbed laser energy, and D is the measured diameter of crater.

3. Results

The spot diameter at the $1/e^2$ position was calculated using the above relation and found to be 49.5 µm. The fluence at which ITO thin film started to change as observed by optical microscopy is defined as the damage threshold, while the value of fluence at which ITO films start to ablate/delaminate is defined

as the ablation threshold. For 50 nm thick film, there was not a significant difference between the damage and ablation thresholds, which were found to be 0.26 Jcm^{-2}. A plot of D^2 verses log of fluence is provided for the 100 nm ITO layer in Figure 1. A fluence of 0.28 Jcm^{-2} and 0.33 Jcm^{-2} were measured as damage and ablation thresholds, respectively, for 100 nm thick ITO. There were no measurable changes induced in the film below 0.26 Jcm^{-2} for 50 nm thick film and 0.28 Jcm^{-2} for 100 nm thick film and fluence values higher than this resulted in physical damage.

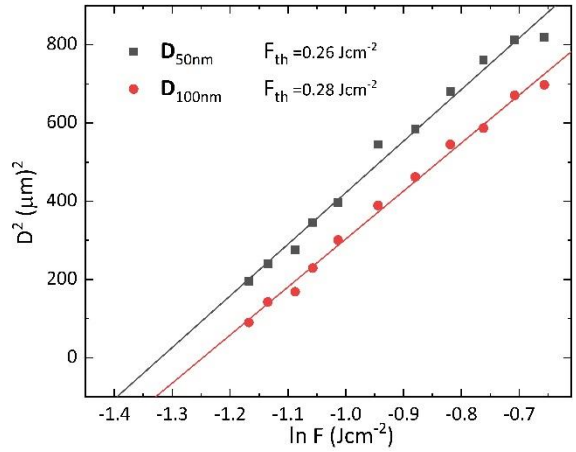

Figure 1: A linear relationship between squared diameter (D^2) and log of applied fluence for 50 nm and 100 nm thick ITO films. Data for 50 nm and 100 nm thick film is presented.

To understand the single pulse ITO thin film ablation, different fluences were used to ablate the thin film. At first, with a single laser pulse at low fluence, damage starts to appear on the surface and then at higher fluence a dome-like structure appeared. The dome-like feature results in the ITO film being ablated or delaminated at fluences of 0.38 Jcm^{-2} and 0.41 Jcm^{-2} for 50 nm and 100 nm, respectively, as provided in Figure 2.

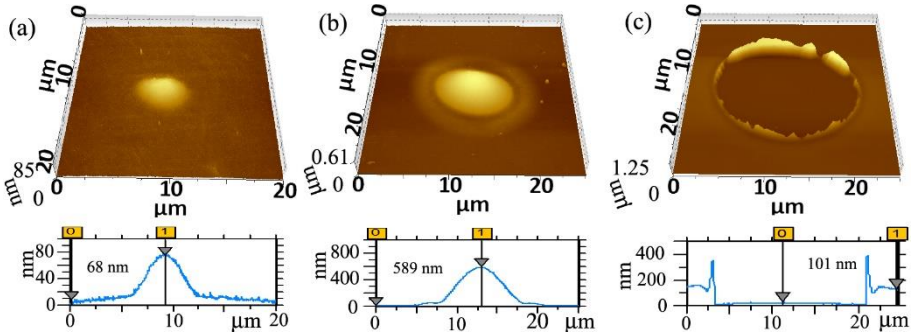

Figure 2: AFM topographic images of 100 nm thick ITO film with single fs laser pulse at (a) 0.36 Jcm^{-2}, (b) 0.41 Jcm^{-2}, and (c) 0.51 Jcm^{-2} and the images at the bottom are their respective surface profiles.

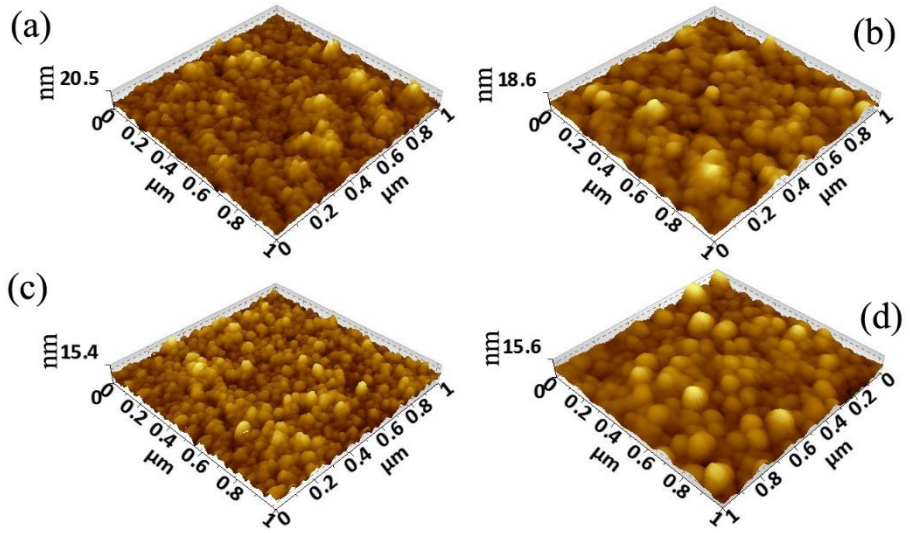

Figure 3: Topographic AFM images of (a) untreated 50 nm thick ITO film and (b) after laser scanning while (c) is untreated 100 nm thin film and (d) is after laser scanning. The samples were scanned at 0.04 Jcm^{-2} with 180 mm/s scan speed which gave 27 SPA and 96% overlapping. A hatching of 5 μm was used.

To enable the improvement in the electrical properties using melt-free or all solid state crystallization, ITO thin films were scanned with high pulse overlapping and laser shots per area (SPA) while using a fluence approximately 7 times smaller than the damage threshold for ITO. A 180 mm/s laser scanning speed was used which gave 27 SPA and 96% pulse overlapping. The laser scanning parameters and fluence values are optimized to avoid any melting and visible damage on the ITO surface. The influence of laser scanning on the surface morphology of the ITO films was investigated by AFM. The topographic AFM images of the ITO films with thicknesses of 50 nm (a, b) and 100 nm (c, d) before and after laser scanning are shown in Figure 3. Before laser irradiation, the ITO films were composed of tiny particles of approximately 20 nm diameter and 45nm diameter for the 50 nm and 100 nm films, respectively. The morphology of the surface was changed due to the laser scanning of the ITO films. The AFM images suggest that nanoparticle sintering has occurred during laser irradiation as shown in Figure 3b and 3d. In this so-called sintering process, the formation of a conductive neck is envisaged to be formed between the nanoparticles resulting in bigger particle sizes within the ITO films. The smaller particles agglomerate to form a larger particle with sizes roughly 60 nm for 50 nm thick film and 80 nm for 100 nm thick films. It is evident from the AFM images that the average particle sizes of the thin films have been increased after the laser scanning for both 50 nm and 100 nm thin films. For 50 nm thin ITO film, root mean square (rms) roughness is improved from 2.56 nm to 2.18 nm after the laser scanning while for 100 nm thin film the rms height increased from 1.87 nm to 2.13 nm because of the overall increase in the particle size. The changes in surface roughness might affect the surface reflection and transmittance of ITO films. It is evident from the AFM images that no melting of ITO thin film is observed in the laser scanning region and the only increase in the grain/particles sizes have occurred by the solid diffusion process.

Surface morphology and electrical properties are interconnected in the case of many thin films. To study the improvement in electrical properties of ITO after laser scanning, a commercial Four-Point Probe System (Ossila UK) was used to measure the sheet resistance of ITO thin films before and after the laser scanning. It was found that the sheet resistance of the 50 nm thin film decreased from 72 Ω/sq to 54 Ω/sq while that for the 100 nm film decreased from 52 to 40 Ω/sq.

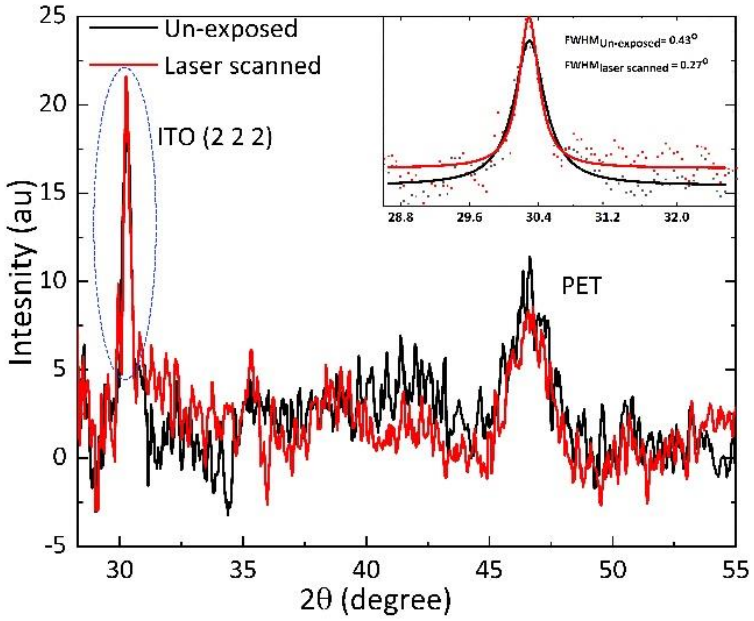

Figure 4: XRD patterns of unexposed and laser exposed ITO thin films of thickness 100 nm in comparison to unirradiated films. The inset of shows the peak fitting of ITO (2 2 2).

In order to investigate if there is a phase change occuring in increasing the grain or particle size which leads to the reduction in the sheet resitance, Bragg-Brentano X-ray diffraction (XRD) analysis of the ITO thin films was performed before and after the laser scanning. Figure 4 shows XRD pattern of irradiated films in comparison to unirradiated films. The XRD analysis confirms the improvement in crystallinity as the peaks from the irradiated ITO film appears to have a reduced full width at half maximum (FWHM). The peak at 46.5° belong to PET substrate. The peak at 30.2° is the only ITO dominant peak that is observed; it is more prominent for the 100 nm thick film compared to 50 nm film. This peak corresponds to the coherent scattering from (2 2 2) reciprocal lattice vector in cubic In_2O_3. The dominant feature shifts to higher angles indicating a lattice contraction due to strain relaxation due to an increase in the substitutional Sn concentration because of the smaller ionic radius of Sn^{4+} compared to In^{3+} and the possible laser induced changes of substitutional to interstitial Sn atoms in the ITO crystal structure [24]. The coherent scattering from ITO (2 2 2) is shown in more detail in inset of Figure 4. This confirms that its FWHM decreases by 37% after laser scanning. The Scherrer relation can be used to estimate the grain size of the film [25]. It is found that the grain size calculated by this way correlates with AFM topographic results for ITO thin films before and after the laser scanning, indicating that the grain size increases from 19 nm to 30 nm. This increase in grain size is attributed to a corresponding increase in particle size by a laser sintering based process.

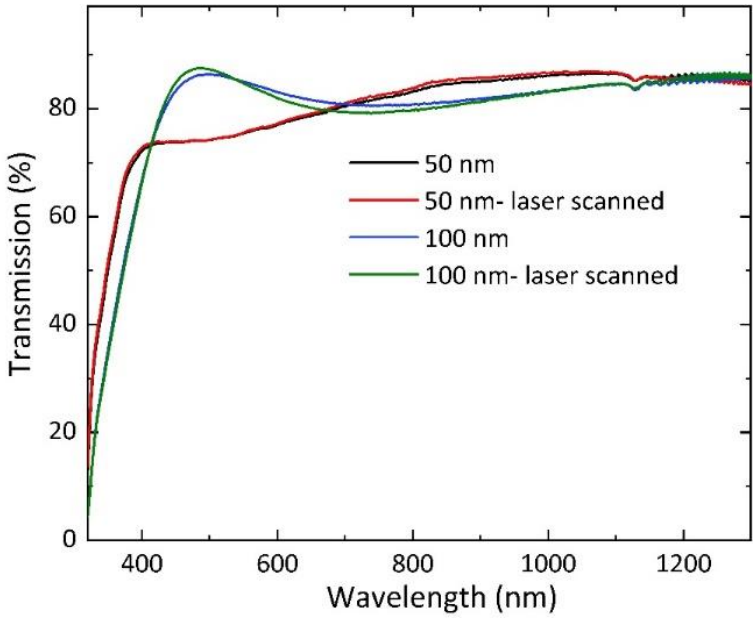

Figure 5: Optical transmittance of the 50 nm and 100 nm thick ITO thin films before and after laser scanning.

ITO thin films microstructures and optical properties are very sensitive to the electrical and crystalline state. The microstructural changes as a result of laser annealing not only affect the electrical but optical properties as well. Higher electrical conductivity of ITO can be achieved but often at the expense of optical transmission. The variation in optical properties such as transmission and band gap energy after the laser scanning were measured by UV-Vis spectrometry. There is an improvement in the average transmittance in the visible region (400-700 nm) after laser scanning for 50 nm and 100 nm thick films as shown in Figure 5. The average transmittance after laser scanning changes from 72.19 to 75.5 % and from 83 to 82.6 % for 50nm and 100 nm thick films, respectively. In the visible region, the transmittance of ITO thin films depends on the degree of crystallinity as the grain boundaries in the thin films scatter the visible light, resulting in lower optical transmittance. The increase in grain size after the laser scanning resulted in a decrease in the number of grain boundaries in ITO thin films. Hence the increase in optical transmission after the laser scanning is due to the improvement in the crystallinity of the thin films as confirmed by AFM and XRD analyses. For the IR region, the interaction of incident radiation with the high density of free electrons in the material cause the decrease in transmission due to enhanced reflectivity. For the UV region, the absorption is due to the fundamental bandgap (E_g) transition. The transparency of ITO thin films exhibits a sharp decrease in the UV region and a shift in absorption edge occurs after laser scanning. The shift of the absorption edge to shorter wavelengths is most likely due to an increase in charge carrier concentration; this effect is known as the Burstein-Moss Shift [26, 27]. The absorption coefficient (α) at different wavelengths is calculated using the transmission and reflectance by the following relation [25];

$$T = (1 - R)\, exp(-\alpha d), \tag{2}$$

where *T*, *R*, and *d*, are the transmission, reflection, and film thickness parameters, respectively. For direct band gap semiconductor, the relation between the absorption coefficient and band gap is given by [28];

$$\alpha(h\nu) = \left(h\nu - E_g\right)^{\frac{1}{2}}, \tag{3}$$

where $h\nu$ is photon energy and E_g is band gap energy. The value of E_g is measured by extrapolations of the linear regions of the plot between $h\nu$ versus $(\alpha h\nu)^2$ to zero absorption (i.e. $\alpha h\nu = 0$). There is change in E_g from 3.90 to 3.91 for 50 nm and 3.92 to 3.94 eV for 100 nm thin film after laser scanning. This

increase in band gap energy is due to an increase in carrier concentration and this change in band gap with change in carrier concentration is related to Burstein-Moss shift. By the definition, the band gap is the energy difference between the top of the valence band and the lowest empty state in the conduction band. Carrier concentration increased after laser scanning resulting in band gap widening due to filling up of the low-lying energy levels in the conduction band.

3.1 Modelling

The dynamics of a free electron in ITO are metal-like and can be described by the Drude model. ITO is an interesting material as recent studies shows it to have a nonlinear response [29]. It was found that the nonlinear response of ITO in the epsilon near zero (ENZ) regime is dominated by free-electrons. This nonlinear mechanism is well described by the so-called delayed two temperature model (TTM). The incident laser energy is absorbed, generates hot electrons with non-thermal energy distribution and act as a delayed heating source. Hence, the response of ultra-short laser interaction with ITO thin film is different from metals. This can be explained by three reasons. Firstly unlike metals, ITO has no interband transition resonance in the visible or infrared range of the optical spectrum; secondly the free-electron density in ITO is smaller than metals resulting in much smaller electron heat capacity, and thirdly the Fermi level is quite low in the conduction band (~1 eV for ITO) due to the relatively small free-electron density. [30]. After absorption from laser pulse, generated hot electrons acquire a non-thermalised energy distribution and act as a delayed source of heating while the lattice is considered cold. The overall dynamics of the conduction electrons and energy transfer to lattice when there exists a thermal non-equilibrium between electrons and phonons is described by a delayed two temperature model [29, 30].

$$C_e \frac{\partial T_e}{\partial t} = \nabla.(k_e \nabla T_e) - G(T_e - T_l) + \frac{N}{2\tau_{ee}}, \tag{4}$$

$$C_l \frac{\partial T_l}{\partial t} = \nabla.(k_l \nabla T_l) + G(T_e - T_l) + \frac{N}{2\tau_{ep}}, \tag{5}$$

$$\frac{\partial N}{\partial t} = -\frac{N}{2\tau_{ee}} - \frac{N}{2\tau_{ep}} + S, \tag{6}$$

$$C_s \frac{\partial T_s}{\partial t} = \nabla.(k_s \nabla T_s), \tag{7}$$

where C_e, C_l are electron and lattice heat capacity, T_e and T_l represents electron and lattice temperature, G (T_e) is electron-phonon coupling factor, N is non-thermal energy density which is stored in excited electrons and S is laser source term, respectively. T_s is the lattice temperature of PET substrate, C_s and K_s are the heat capacity and thermal conductivity respectively.

Equation (7) represents the lattice heat diffusion from ITO thin to the PET substrates. The energy transport at the ITO-PET interface is accounted by considering the interaction between electrons in ITO thin film with phonons in the PET substrate using the boundary condition as;

$$(T_s - T_e^{ITO})|_{z=d} = k_e^{ITO} R_{es} \left.\frac{\partial T_e^{ITO}}{\partial z}\right|_{z=d}$$

where T_s is PET temperature and R_{es} is the thermal boundary resistance.

The electron phonon coupling factor ($G(T_e)$) describes the strength of energy transfer between the excited electrons and lattice vibrational modes of ITO and can be estimated as [31];

$$G(T_e) = \frac{\pi^2 m_e^* v_s n_e}{6\tau(T_e)T_e} \tag{8}$$

where m_e^* is effective electron mass, v_s is speed of sound, n_e is free electron density, and τ is the temperature dependent relaxation time. Electron-electron collisions lead to an energy relaxation within the electron gas called thermalization and the mean time required for electrons to change their states is termed as electron-electron relaxation time (τ_{ee}). Through this process of electron-electron collisions, the absorbed energy is re-distributed among the free electrons resulting in electron gas thermal equilibrium and thus to a Fermi distribution [32]. In other words, τ_{ee} is measure of redistribution of energy to the electrons and is given by [33];

$$\frac{1}{\tau_{ee}} = \frac{\pi(k_B T_e)^2}{(8\hbar E_F)} + \frac{\sqrt{3}}{2\hbar\sqrt{E_F}}\left(\frac{k_B T}{k_F l}\right)^{3/2} \tag{9}$$

where, K_B is Boltzmann constant, T_e is electron temperature, ħ is reduced Plank constant, E_F is Fermi energy, k_F is Fermi wavenumber and l is electrons mean free path. Electron-phonon relaxation time (τ_{ep}) can be estimated by electron-phonon coupling factor and the temperature dependent specific heat capacity of free electrons as [29];

$$\tau_{ep} = 2\frac{C_e(T_e)}{G(T_e)} \tag{10}$$

For T_l much smaller than Debye temperature (T_D), the number of interacting phonon modes and the lattice heat capacity (C_l) is a function of lattice temperature (T_l) and asymptotically approaches a constant value as T_l approaches T_D, the temperature of highest mode of vibration of lattice. We used the temperature dependent values of C_e and C_l in our model as provided in Figure 6(a,b), reported in the supplementary information of [34].

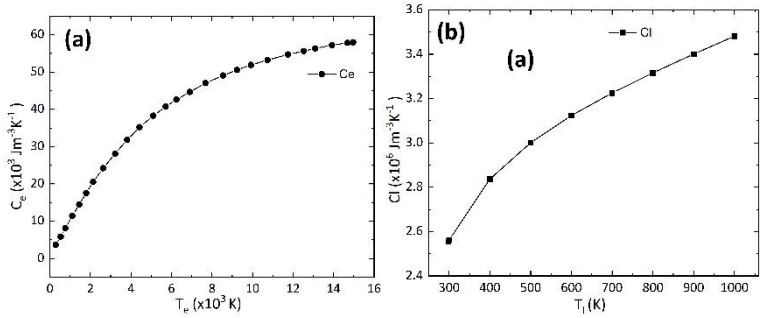

Figure 6: Temperature dependent (a) electrons heat capacity and (b) lattice heat capacity of ITO used in modelling.

The temporal and volumetric energy from the laser source of Gaussian profile can be defined as;

$$S(\boldsymbol{r},t) = \frac{\alpha \times 0.94 \times \varphi_0 \times (1-R)}{t_p} exp\left\{\frac{-2x^2}{\omega_o^2} - 4In2\left(\frac{t-t_r}{t_p}\right)^2\right\} exp(-z\alpha) \tag{11}$$

here α is wavelength dependent absorption coefficient, φ_0 is laser fluence, R is reflectivity of material, t_p is laser pulse duration, ω_o is beam radius, t is time, t_r is reference time. Thermophysical parameters used in simulation are provided in table 2 and 3.

In ultra-short laser interactions, electrons re-establish the Fermi distribution after the absorption of the energy from the laser pulse while the lattice remains at the same temperature. Initially excited electrons are localized within the optical absorption depth and diffuse into deeper parts due to

established temperature gradient. Electron relaxation time characterizes whether the transport of electrons is diffusive or ballistic while electron-phonon coupling defines the diffusion length of electrons into sample. Thermal electrons transfer energy to lattice through electron-phonon coupling and establish electron-phonon equilibrium. The simulation results describing the evolution of electron and lattice temperatures are presented in Figure 7; the fluence used corresponds to the values used in the XRD results.

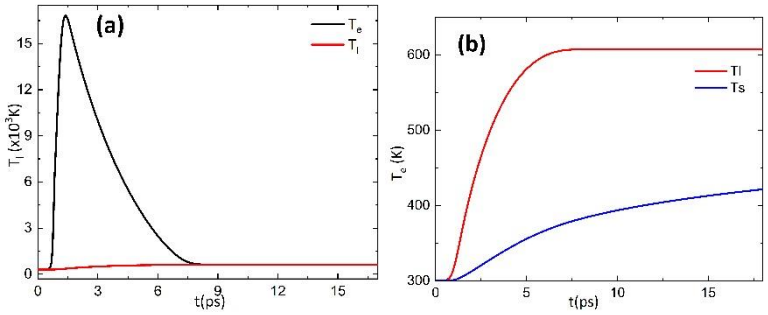

Figure 7: (a) shows the numerical simulation results for femtosecond laser induced the evolution of electrons and lattice temperature for 100 nm ITO thin film on PET substrate as function of time at a fluence of 0.04 Jcm^{-2}. (b) Comparison of ITO lattice temperature and PET substrate temperature at the ITO-PET interface.

The model predicts that the electron temperature rises fast because of their lower heat capacity compared to the lattice. The lattice temperature rises after the electron-phonon coupling starts. At fluence of 0.04 Jcm^{-2}, a maximum lattice temperature of 608 K was observed while the electron temperature peaks at 16800 K at 1.39 ps after the onset of the laser pulse. Thermal electron-lattice equilibrium was established at 8.4 ps. A maximum temperature of 420 K at the PET surface was observed which proves that ITO crystallization process completed without damaging the lower PET surface. While, at a fluence of ablation threshold (0.33 Jcm^{-2}) for 100 nm ITO thin film, model predicts maximum lattice temperature of 1380 K while PET surface temperature was 715 K. This suggests that the ablation/damage of ITO was not because of melting or vaporization but due to different thermal expansion rate resulting in stress generation. The coefficient of thermal expansion of ITO ($7.2x10^{-6}$ K^{-1}) is about 10 times lower than of PET ($70x10^{-6}$ K^{-1}).

Table 1: Thermodynamical and optical properties parameters of ITO and PET used in modelling.

Parameter	**Value**
Debye temperature of ITO (T_D)	1000 K [30]
Melting temperature of ITO (T_m)	2100 K
Lattice thermal conductivity of ITO (K_l)	3.95 W $m^{-1}K^{-1}$ [35]
Electron thermal conductivity ITO (K_e)	1.4 W $m^{-1}K^{-1}$ [36] at 300 K
Lattice heat capacity of ITO (C_l)	2.6 x 10^6 $Jm^{-3}K^{-1}$ @300K [30]
Electron heat capacity of ITO (C_e)	4.53 $Jm^{-3}K^{-1}$
Fermi velocity of ITO (v_F)	1.0x10^6 ms^{-1} [33]
Fermi energy of ITO (E_F)	1.0 eV [33]
Fermi wavenumber of ITO (k_F)	3.1x10^9 m^{-1}
Electron mean free path of ITO	8.3 nm
Effective mass of electron (m*)	0.35 m_e
Free electron number density of ITO (n)	1x10^{21} cm^{-3}
Speed of sound in ITO film (C_s)	4354 ms^{-1} [37]
Density of ITO (ρ)	7120 kg/m^{-3}
Heat capacity of PET (C_s)	1.42x10^3 $Jm^{-3}K^{-1}$
Thermal conductivity (k_s)	0.261 $Wm^{-1}K^{-1}$
Melting point of PET (T_{m-s})	533 K
Density of PET (ρ_s)	1.42 kg m^{-3}

3. Discussion

We have observed up to 23 % improvement in conductivity for 50 nm and a 25% increase in 100 nm thick ITO thin films after the laser scanning. AFM characterization confirms an increase in average particle size after laser treatment, combined with a significant improvement in crystallinity as confirmed by XRD characterization. Transmission measurements are supportive of a more crystallised thin film. Simulation results predicts that crystallization occurred at low temperatures without melting of ITO and damage to the underlying PET substrate. It is well the conductivity arises due to the charge carriers

provided by Sn dopants and oxygen vacancies in ITO [38]. The conduction mechanism in amorphous ITO thin films, deposited at low temperature, is via the donation of electrons generated by the oxygen vacancies. It has been reported that when annealed at atmosphere, oxygen in the air reacts with the ITO films; the resulting decrease in density of oxygen vacancies reduces the free carrier concentration which in turn leads to an increase in the resistivity. However, in vacuum, there is less or no oxygen reaction with the ITO film surface, and even in vacuum oxygen atoms desorbed from the surface can escape to increase the carrier concentration [39]. Even though the laser scanning in our work was done in atmosphere, we too must also consider oxygen removal and resulting oxygen vacancy generation along with the proposed improvement in crystallization; together they result in an improvement in conductivity during and after the laser scanning. In case of 50 nm thick ITO films, it is probable that oxygen vacancy generation leading to higher conductivity is the main mechanism. Obvious XRD peak changes due to substitutional Sn can be seen from the XRD data for 100 nm ITO film but no obvious XRD changes were found for the 50nm thick ITO film. It is likely that the as-deposited ITO film on PET is not well crystallized, so the 50nm ITO is too thin and too amorphous to observe the XRD characteristic peaks of ITO.

In ultra-short laser pulse semiconductor interaction, laser energy is transferred first to the electrons and then to the lattice. After laser irradiation, the semiconductor undergoes several stages before returning to equilibrium; these stages include carrier excitation, thermalization of carriers with themselves, thermalization of carriers with the lattice, carrier removal and thermal/structural changes [40]. If the photon energy is greater than the bandgap, then single photon absorption is the dominant mechanism for excitation of valence electrons to the conduction band. However, if the direct band gap (3.1 eV for ITO) is greater than the infrared laser photon energy (1.2 eV for IR photons), then multiphoton absorption is the most likely main excitation mechanism. If there are free carriers in the semiconductor, then free carrier absorption increases the energy of carriers in the electron (and hole) plasma dominates as it does in metals. The number density of free carriers does not change with absorption, but the energy of the free carrier gas is increased. If the laser energy is high enough to cause the excitation of free carriers above the bandgap (for a semiconductor) or above the Fermi level (for a metal) then impact ionization can generate additional excited carriers [41].

Covalent bonding is dominant for ITO and it is stable only if the electrons are in the ground state. However, this covalent bonding breaks down on excitation of electrons from stable valence band states to antibonding conduction states. If enough electrons populate the antibonding states in the conduction band during ultra-short pulse excitation, the lattice structure will become unstable; the cohesive energy of the lattice will be reduced by bond breaking. It has been reported that if 10% of the valence electrons are excited, the lattice begins to deform due to the softening of certain phonon modes [41]. Hence it is plausible that an ultra-short laser pulse can induce such a lattice instability by dense photo-excited plasmas which weaken the lattice and thereby promote the ion movement over a significant fraction of the bond length without significantly increasing their thermal energy [42]. Therefore, we propose the weakening of the lattice by high density electron and hole plasmas to be the main mechanism for the non-thermal phase change in femtosecond laser annealing of ITO.

4. Conclusion

This study reports on improvements in the electrical properties and crystallization of very thin films on a heat sensitive PET substrate by ultra-short laser scanning. The experimental results have demonstrated that non-melting crystallization of ITO was performed at a fluence seven times smaller than the damage threshold of ITO films. An analysis of surface morphology revealed enhancement in the films grain size after laser scanning while XRD confirms the requisite improved crystallinity. We proposed ultra-short laser non-melt crystallization based on solid diffusion at low fluence. A decrease up to 25 % in sheet resistance was measured after laser scanning. The hypothesis for low temperature solid state crystallisation is supported by the predications obtained in the delayed two temperature numerical model; simulations predict that the lattice temperatures only reach ~33% of the reported melt temperature for the ITO lattice. Thus, low fluence ultra-short laser crystallization could be useful in crystallization of thin films on a heat sensitive substrate. This process offers a selective crystallization in remote regions without effecting the nearby components.

Funding
The work was jointly supported by two research grants from Science Foundation Ireland (SFI) and is co-funded under the European Regional Development Fund under Grant Numbers 12/RC/2276 and 16/RC/3872.

References

[1] Zoski C G 2006 *Handbook of electrochemistry*: Elsevier)
[2] Satoh T, Fujikawa H and Taga Y 2005 Influence of indium tin oxide electrodes deposited at room temperature on the properties of organic light-emitting devices *Applied Physics Letters* **87** 143503
[3] Betz U, Olsson M K, Marthy J, Escolá M and Atamny F 2006 Thin films engineering of indium tin oxide: large area flat panel displays application *Surface and Coatings Technology* **200** 5751-9
[4] Maheshwari V and Saraf R F 2006 High-Resolution Thin-Film Device to Sense Texture by Touch *Science* **312** 1501
[5] Yoshimura M, Nakai E, Tomioka K and Fukui T 2013 Indium tin oxide and indium phosphide heterojunction nanowire array solar cells *Applied Physics Letters* **103** 243111
[6] Ginley D S and Bright C 2000 Transparent conducting oxides *MRS bulletin* **25** 15-8
[7] Horng R-H, Wuu D-S, Lien Y-C and Lan W-H 2001 Low-resistance and high-transparency Ni/indium tin oxide ohmic contacts to p-type GaN *Applied Physics Letters* **79** 2925-7
[8] Maruyama T and Fukui K 1991 Indium tin oxide thin films prepared by chemical vapour deposition *Thin Solid Films* **203** 297-302
[9] Granqvist C G and Hultåker A 2002 Transparent and conducting ITO films: new developments and applications *Thin Solid Films* **411** 1-5
[10] Vasu V and Subrahmanyam A 1990 Reaction kinetics of the formation of indium tin oxide films grown by spray pyrolysis *Thin Solid Films* **193-194** 696-703
[11] Cruz L R, Legnani C, Matoso I G, Ferreira C L and Moutinho H R 2004 Influence of pressure and annealing on the microstructural and electro-optical properties of RF magnetron sputtered ITO thin films *Materials Research Bulletin* **39** 993-1003
[12] Serkov A A, Snelling H V, Heusing S and Amaral T M 2019 Laser sintering of gravure printed indium tin oxide films on polyethylene terephthalate for flexible electronics *Scientific Reports* **9** 1773
[13] Hu Y, Diao X, Wang C, Hao W and Wang T 2004 Effects of heat treatment on properties of ITO films prepared by rf magnetron sputtering *Vacuum* **75** 183-8
[14] Sameshima T, Usui S and Sekiya M 1986 XeCl Excimer laser annealing used in the fabrication of poly-Si TFT's *IEEE Electron Device Letters* **7** 276-8
[15] Chae J, Jang L and Jain K 2010 High-resolution, resistless patterning of indium-tin-oxide thin films using excimer laser projection annealing process *Materials Letters* **64** 948-50
[16] Farid N, Chan H, Milne D, Brunton A and M. O'Connor G 2018 Stress assisted selective ablation of ITO thin film by picosecond laser *Applied Surface Science* **427** 499-504
[17] Farid N, Dasgupta P and O'Connor G M 2018 Onset and evolution of laser induced periodic surface structures on indium tin oxide thin films for clean ablation using a repetitively pulsed picosecond laser at low fluence *Journal of Physics D: Applied Physics* **51** 155104
[18] Cheng C W L I M and Chen J S 2014 Femtosecond laser-induced nanoperiodic structures and simultaneous crystallization in amorphous indium-tin-oxide thin films *Appl. Surf. Sci.* **316** 9
[19] Hoppius J S, Bialuschewski D, Mathur S, Ostendorf A and Gurevich E L 2018 Femtosecond laser crystallization of amorphous titanium oxide thin films *Applied Physics Letters* **113** 071904
[20] Cheng C-W, ing Lin C-Y, Shen W-C, Lee Y-J and Chen J-S 2010 Patterning crystalline indium tin oxide by high repetition rate femtosecond laser-induced crystallization *Thin Solid Films* **518** 7138-42
[21] Thakur V K, Ding G, Ma J, Lee P S and Lu X 2012 Hybrid Materials and Polymer Electrolytes for Electrochromic Device Applications *Advanced Materials* **24** 4071-96

[22] Ahn M H, Cho E S and Kwon S J 2014 Characteristics of ITO-resistive touch film deposited on a PET substrate by in-line DC magnetron sputtering *Vacuum* **101** 221-7
[23] Liu J M 1982 Simple technique for measurements of pulsed Gaussian-beam spot sizes *Opt. Lett.* **7** 196-8
[24] Shigesato Y, Hayashi Y and Haranoh T 1992 Doping mechanisms of tin-doped indium oxide films *Applied Physics Letters* **61** 73-5
[25] Kim H, Gilmore C M, Piqué A, Horwitz J S, Mattoussi H, Murata H, Kafafi Z H and Chrisey D B 1999 Electrical, optical, and structural properties of indium–tin–oxide thin films for organic light-emitting devices *Journal of Applied Physics* **86** 6451-61
[26] Burstein E 1954 Anomalous Optical Absorption Limit in InSb *Physical Review* **93** 632-3
[27] Moss T S 1954 The Interpretation of the Properties of Indium Antimonide *Proceedings of the Physical Society. Section B* **67** 775-82
[28] Tauc J, Grigorovici R and Vancu A 1966 Optical Properties and Electronic Structure of Amorphous Germanium *physica status solidi (b)* **15** 627-37
[29] Alam M Z, Schulz S A, Upham J, De Leon I and Boyd R W 2018 Large optical nonlinearity of nanoantennas coupled to an epsilon-near-zero material *Nature Photonics* **12** 79-83
[30] Alam M Z, De Leon I and Boyd R W 2016 Large optical nonlinearity of indium tin oxide in its epsilon-near-zero region *Science* **352** 795
[31] Jiang L and Tsai H-L 2005 Improved Two-Temperature Model and Its Application in Ultrashort Laser Heating of Metal Films *Journal of Heat Transfer* **127** 1167-73
[32] Rethfeld B, Kaiser A, Vicanek M and Simon G 2002 Ultrafast dynamics of nonequilibrium electrons in metals under femtosecond laser irradiation *Physical Review B* **65** 214303
[33] Lin J-J and Li Z-Q 2014 Electronic conduction properties of indium tin oxide: single-particle and many-body transport *Journal of Physics: Condensed Matter* **26** 343201
[34] Guo P, Schaller R D, Ocola L E, Diroll B T, Ketterson J B and Chang R P H 2016 Large optical nonlinearity of ITO nanorods for sub-picosecond all-optical modulation of the full-visible spectrum *Nature Communications* **7** 12892
[35] Guo P, Schaller R D, Ketterson J B and Chang R P H 2016 Ultrafast switching of tunable infrared plasmons in indium tin oxide nanorod arrays with large absolute amplitude *Nature Photonics* **10** 267-73
[36] Yagi T, Tamano K, Sato Y, Taketoshi N, Baba T and Shigesato Y 2005 Analysis on thermal properties of tin doped indium oxide films by picosecond thermoreflectance measurement *Journal of Vacuum Science & Technology A* **23** 1180-6
[37] Ashida T, Miyamura A, Oka N, Sato Y, Yagi T, Taketoshi N, Baba T and Shigesato Y 2009 Thermal transport properties of polycrystalline tin-doped indium oxide films *Journal of Applied Physics* **105** 073709
[38] Bhagwat S and Howson R P 1999 Use of the magnetron-sputtering technique for the control of the properties of indium tin oxide thin films *Surface and Coatings Technology* **111** 163-71
[39] Shigesato Y and Paine D C 1993 Study of the effect of Sn doping on the electronic transport properties of thin film indium oxide *Applied Physics Letters* **62** 1268-70
[40] Sundaram S K and Mazur E 2002 Inducing and probing non-thermal transitions in semiconductors using femtosecond laser pulses *Nature Materials* **1** 217-24
[41] Y Siegal, E N Glezer, L Huang a and Mazur E 1995 Laser-Induced Phase Transitions in Semiconductors *Annual Review of Materials Science* **25** 223-47
[42] Bang J, Sun Y Y, Liu X Q, Gao F and Zhang S B 2016 Carrier-Multiplication-Induced Structural Change during Ultrafast Carrier Relaxation and Nonthermal Phase Transition in Semiconductors *Physical Review Letters* **117** 126402

Figure Captions

Figure 1: A linear relationship between squared diameter (D^2) and log of applied fluence for 50 nm and 100 nm thick ITO films. Data for 50 nm and 100 nm thick film is presented.

Figure 2: AFM topographic images of 100 nm thick ITO film with single fs laser pulse at (a) 0.36 Jcm^{-2}, (b) 0.41 Jcm^{-2}, and (c) 0.51 Jcm^{-2} and the images at the bottom are their respective surface profiles.

Figure 3: Topographic AFM images of (a) untreated 50 nm thick ITO film and (b) after laser scanning while (c) is untreated 100 nm thin film and (d) is after laser scanning. The samples were scanned at 0.04 Jcm^{-2} with 180 mm/s scan speed which gave 27 SPA and 96% overlapping. A hatching of 5 μm was used.

Figure 4: XRD patterns of unexposed and laser exposed ITO thin films of thickness 100 nm in comparison to unirradiated films. The inset of shows the peak fitting of ITO (2 2 2).

Figure 5: Optical transmittance of the 50 nm and 100 nm thick ITO thin films before and after laser scanning.

Figure 6: Temperature dependent (a) electrons heat capacity and (b) lattice heat capacity of ITO.

Figure 7: (a) shows the numerical simulation results for femtosecond laser induced the evolution of electrons and lattice temperature for 100 nm ITO thin film on PET substrate as function of time at a fluence of 0.04 Jcm^{-2}. (b) Comparison of ITO lattice temperature and PET substrate temperature at the ITO-PET interface.

Table caption

Table 1: Thermodynamical and optical properties parameters of ITO and PET used in modelling.

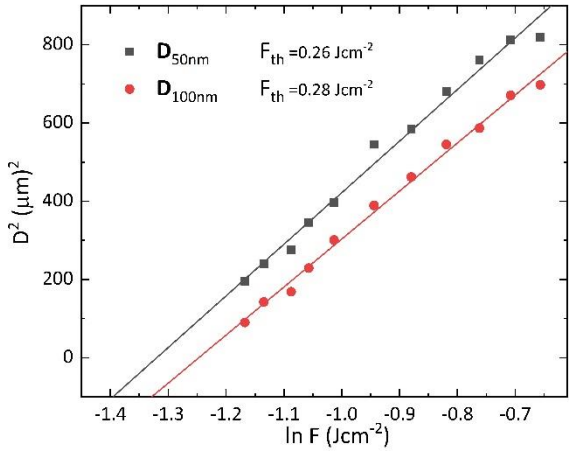

Figure 1

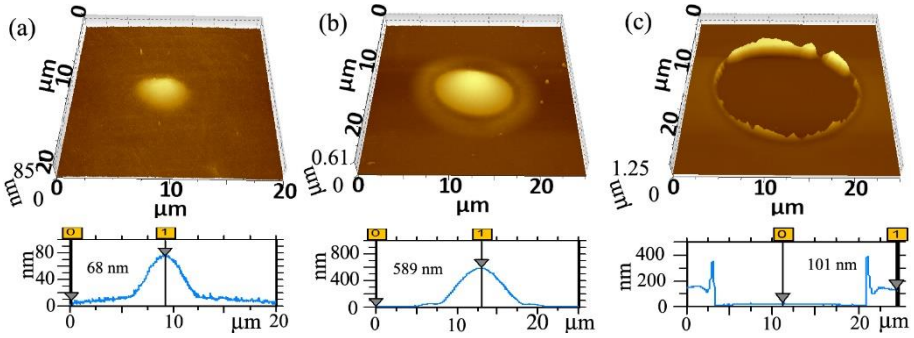

Figure 2

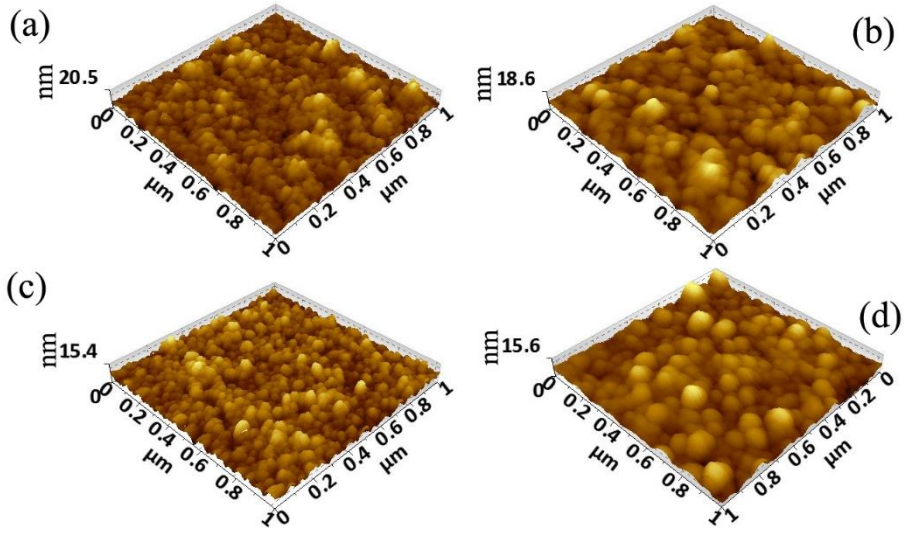

Figure 3

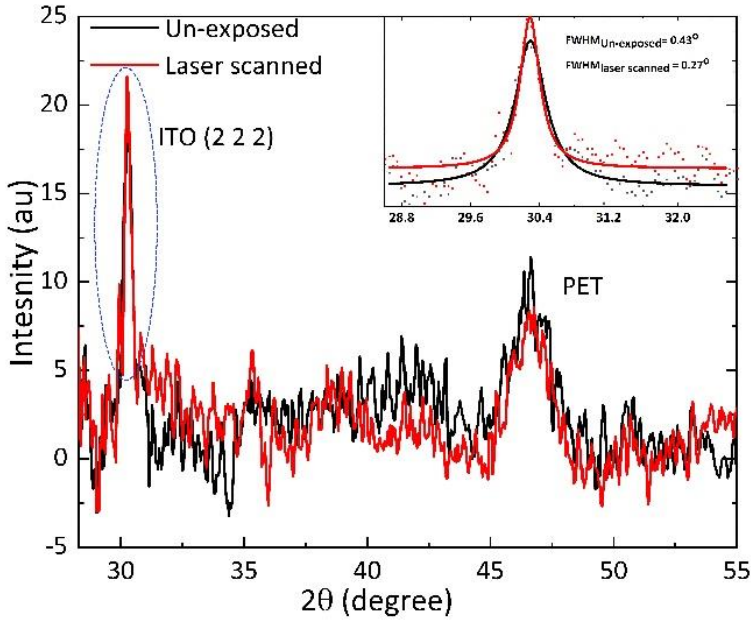

Figure 4

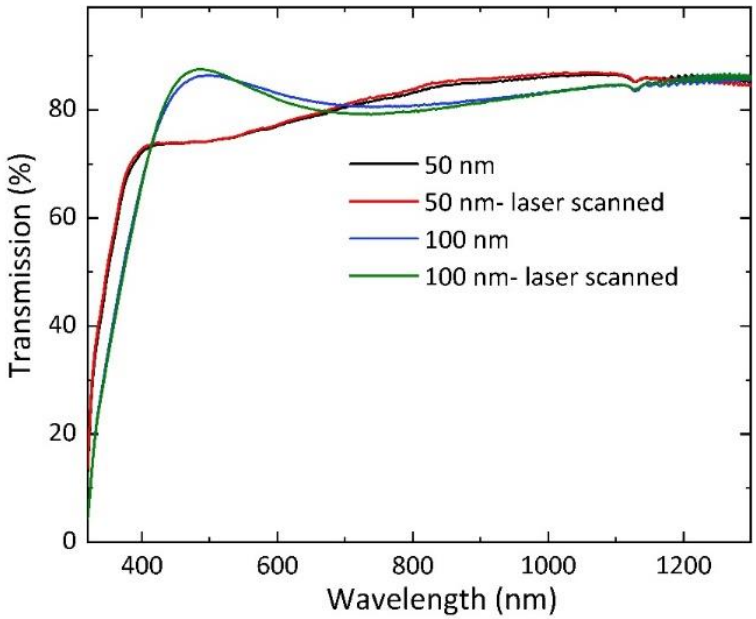

Figure 5

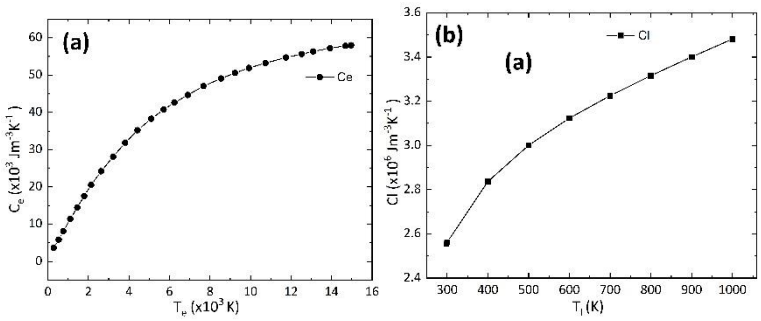

Figure 6

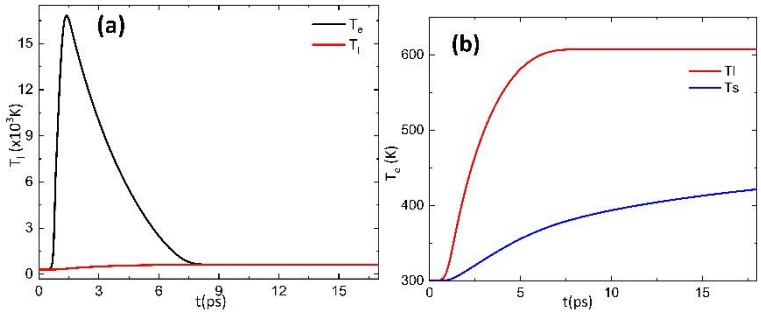

Figure 7

Table 1

Parameter	**Value**
Debye temperature of ITO (T_D)	1000 K [30]
Melting temperature of ITO (T_m)	2100 K
Lattice thermal conductivity of ITO (K_l)	3.95 W $m^{-1}K^{-1}$ [35]
Electron thermal conductivity ITO (K_e)	1.4 W $m^{-1}K^{-1}$ [36] at 300 K
Lattice heat capacity of ITO (C_l)	2.6 x 10^6 $Jm^{-3}K^{-1}$ @300K [30]
Electron heat capacity of ITO (C_e)	4.53 $Jm^{-3}K^{-1}$
Fermi velocity of ITO (v_F)	1.0x10^6 ms^{-1} [33]
Fermi energy of ITO (E_F)	1.0 eV [33]
Fermi wavenumber of ITO (k_F)	3.1x10^9 m^{-1}
Electron mean free path of ITO	8.3 nm
Effective mass of electron (m*)	0.35 m_e
Free electron number density of ITO (n)	1x10^{21} cm^{-3}
Speed of sound in ITO film (C_s)	4354 ms^{-1} [37]
Density of ITO (ρ)	7120 kg/m^{-3}
Heat capacity of PET (C_s)	1.42x10^3 $Jm^{-3}K^{-1}$
Thermal conductivity (k_s)	0.261 $Wm^{-1}K^{-1}$
Melting point of PET (T_{m-s})	533 K
Density of PET (ρ_{PET})	1.42 kg m^{-3}